PHOTONICS Research

Miniaturized and highly sensitive fiber-optic Fabry–Perot sensor for mHz infrasound detection

PEIJIE WANG,[1,2,†] YUFENG PAN,[1,2,†] JIANGSHAN ZHANG,[3] JIE ZHAI,[1,2] DEMING LIU,[1,2] AND PING LU[1,2,*]

[1]*Wuhan National Laboratory for Optoelectronics (WNLO) and National Engineering Research Center of Next Generation Internet Access System, School of Optical and Electronic Information, Huazhong University of Science and Technology, Wuhan 430074, China*
[2]*Optics Valley Laboratory, Wuhan 430074, China*
[3]*Department of Electronics and Information Engineering, Huazhong University of Science and Technology, Wuhan 430074, China*
[†]*These authors contributed equally to this work.*
*Corresponding author: pluriver@mail.hust.edu.cn

Infrasound detection is important in natural disasters monitoring, military defense, underwater acoustic detection, and other domains. Fiber-optic Fabry–Perot (FP) acoustic sensors have the advantages of small structure size, long-distance detection, immunity to electromagnetic interference, and so on. The size of an FP sensor depends on the transducer diaphragm size and the back cavity volume. However, a small transducer diaphragm size means a low sensitivity. Moreover, a small back cavity volume will increase the low cut-off frequency of the sensor. Hence, it is difficult for fiber-optic FP infrasound sensors to simultaneously achieve miniaturization, high sensitivity, and extremely low detectable frequency. In this work, we proposed and demonstrated a miniaturized and highly sensitive fiber-optic FP sensor for mHz infrasound detection by exploiting a Cr-Ag-Au composite acoustic-optic transducer diaphragm and a MEMS technique-based spiral micro-flow hole. The use of the spiral micro-flow hole as the connecting hole greatly reduced the volume of the sensor and decreased the low-frequency limit, while the back cavity volume was not increased. Combined with the Cr-Ag-Au composite diaphragm, a detection sensitivity of −123.19 dB re 1 rad/µPa at 5 Hz and a minimum detectable pressure (MDP) of 1.2 mPa/Hz$^{1/2}$ at 5 Hz were achieved. The low detectable frequency can reach 0.01 Hz and the flat response range was 0.01–2500 Hz with a sensitivity fluctuation of ±1.5 dB. Moreover, the size of the designed sensor was only 12 mm × Φ12.7 mm. These excellent characteristics make the sensor have great practical application prospects.   © 2024 Chinese Laser Press

https://doi.org/10.1364/PRJ.519946

1. INTRODUCTION

Infrasound waves are widely present in nature, with frequencies below the threshold of human hearing (<20 Hz) [1]. Before some natural disasters occur, infrasound waves are generated, such as seismic activity [2–5], volcanic eruptions [6], debris flows [7,8], and snow avalanches [9,10]. Hence, early warning of disasters can be achieved by detecting the infrasound waves. In the military field, infrasound waves have been used as an attack weapon since they can resonate with certain organs of the human body, and thus infrasound detection/defense is also essential. On the other hand, pipeline leakage monitoring [11,12] and underwater acoustic detection [13,14] also include the infrasound frequency band. Therefore, the development of infrasound sensors is crucial for practical applications and is moving toward miniaturization, high performance, and intelligence. Different principle-based infrasound sensors transpose the infrasound signals into different measurable physical quantities through the implementation of various energy conversion mechanisms such as capacitive, piezoelectric, and optical inter-

ference [15]. In recent years, the establishment of the International Monitoring System (IMS) infrasound network has resulted in unprecedented advancements in infrasound research [16]. The commercial electrical infrasound sensor (Martec MB2005) was applied to the IMS for the Comprehensive Nuclear-Test-Ban Treaty. However, although electrical infrasound sensors are convenient to use, they are susceptible to electromagnetic interference, difficult to achieve long-distance detection and multiplexing networking [17], which limits their application in certain specific fields, such as pipeline leakage monitoring and underwater acoustic detection [18].

Fiber-optic Fabry–Perot (FP) acoustic sensors, based on the optical FP interference principle, have the advantages of high sensitivity, small structure size, long-distance detection, immunity to electromagnetic interference, easy to multiplexing networking, and so on [19–27]. For an FP acoustic sensor, acoustic-optic transducer diaphragms of various materials were usually considered to improve the detection sensitivity of acoustic pressure response, such as metallic diaphragms [28–31],

silicon-related diaphragms [32–34], polymer diaphragms [35,36], two-dimensional materials diaphragms [37–40], and special structure diaphragms [41–44]. On the other hand, the detection sensitivity is directly proportional to the size of the diaphragm. When pursuing miniaturized sensors, the detection sensitivity will be sacrificed due to the small diaphragm size. Furthermore, the detection sensitivity of the sensor is not only constrained by the materials and sizes of transducer diaphragms but also depends on the back cavity structures, which are designed to improve the response characteristics and balance the influence of the environmental factors such as temperature. For infrasound detection, to decrease the low cut-off frequency, the back cavity volume can be increased, but this will also increase the size of the sensor. Another optional approach is mechanical filtering [45,46]. In 2021, Zhang *et al.* reported a fiber-optic FP sensor for 0.01 Hz infrasound detection by connecting the capillary glass tube through the pressure difference mechanical filtering device. The size of the capillary tube and the back cavity jointly restrict the low cut-off frequency. Nevertheless, the limitation of capillary tube length leads to an increase in the back cavity volume and the sensor size, resulting in a very large size of >20 cm $\times \Phi 8$ cm. In addition, the frequency response range of the sensor was only 0.01–1 Hz [46]. Therefore, for infrasound detection, it is a challenge for fiber-optic FP sensors to simultaneously achieve miniaturization, high sensitivity, and extremely low detectable frequency.

In this work, a fiber-optic FP sensor with a very small size of 12 mm $\times \Phi 12.7$ mm was proposed and demonstrated for highly sensitive mHz infrasound detection. A chromium-silver-gold (Cr-Ag-Au) composite metal diaphragm was selected as the acoustic-optic transducer diaphragm, which has high sensitivity and stable performance. To decrease the low cut-off frequency and reduce the sensor size, the equivalent circuit of the acoustic sensing system was analyzed, and a miniaturized spiral micro-flow hole was designed and fabricated by micro electromechanical system (MEMS) technique to be employed as the connecting hole with a long length. The low detectable frequency can reach 0.01 Hz and the flat response range was from 0.01 to 2500 Hz with a sensitivity fluctuation of ± 1.5 dB. The infrasound signals were demodulated accurately in real time by using the white light interferometry (WLI) Fourier phase demodulation method. The achieved performances of the designed sensor were superior with respect to the reported results, in terms of acoustic pressure sensitivity, minimum detectable pressure (MDP), and low detectable frequency as well as sensor size. Such an infrasound sensor provides a promising solution for the application in natural disaster warning, underwater acoustic detection, pipeline monitoring, and other domains.

2. PRINCIPLES AND SIMULATION

A schematic diagram of the proposed fiber-optic FP acoustic sensor is shown in Fig. 1(a). The end surface of the fiber and the transducer diaphragm formed an FP interference resonator (FP cavity), which can be simplified as a two-beam interferometer due to the low reflectivity of the fiber end surface. When the acoustic wave acts on the sensitive transducer diaphragm, the diaphragm is elastically deformed, and thus the reflection interference spectrum is modulated by the acoustic wave.

When the thin diaphragm vibrates, the edge experiences minimal displacement while the center experiences maximum since the surrounding of the diaphragm is clamped. For an FP sensor, the fiber end surface must align with the diaphragm center to determine the displacement sensitivity of the diaphragm by calculating the ratio of the shape variable at the midpoint to the applied acoustic pressure. The diaphragm's tension is $T = Ph$, where P represents the tensile stress and h represents the thickness, and the sensitivity can be expressed as [47]

$$S_d = \frac{1}{k^2 Ph}\left[\frac{1}{J_0(ka)} - 1\right],\tag{1}$$

where $k = \omega/c$, $J_0(ka)$ is the zeroth-order Bezier function, and a is the radius of the diaphragm. As a result, to improve the sensitivity, the thickness and the tensile stress of the diaphragm should be decreased, and the radius of the diaphragm should be increased. The complete theoretical model of diaphragm vibration is depicted in Appendix A.

When selecting diaphragm materials, theoretical analysis and calculations were conducted. On the other hand, for silicon-related diaphragms or polymer diaphragms, due to their low reflectivity, a layer of metal needs to be coated on them to
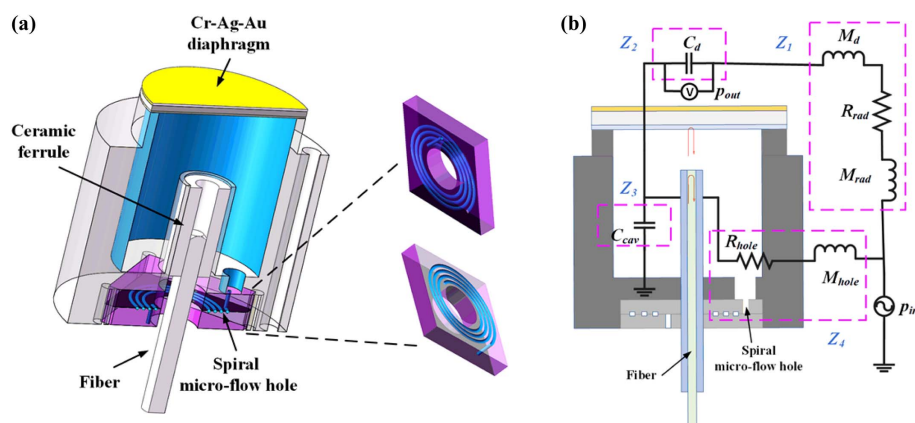

Fig. 1. (a) Schematic diagram of the fiber-optic FP acoustic sensor. (b) Electrical-mechanical-acoustic equivalent model of the sensor.

improve reflectivity, which undoubtedly increases the production cost and process difficulty. As for two-dimensional materials, such as graphene, the large-scale preparation and the consistency of sensors are difficult to guarantee. By the calculation and simulation of diaphragm vibration theory, the Cr-Ag-Au composite metal diaphragm was selected as the acoustic-optic transducer diaphragm, which has high sensitivity and stable performance. Cr was selected as the bottom layer because Cr has excellent corrosion resistance and wear resistance, and Cr was easier to grow on the photoresist during evaporation. The temperature of Ag can be kept at a constant level at a low temperature during the coating process, which can control the residual thermal stress of the diaphragm caused by temperature change. As a result, the aggregation of thermal stress can be reduced, and thus the sensitivity can be further improved. Consequently, Ag was selected as the main deformation layer. However, Ag is prone to oxidation in the air to form silver oxide, which can affect the stability of the sensor performance. Hence, a layer of Au diaphragm was evaporated on the upper layer due to the good chemical stability of Au. In addition, Au can provide a high reflectivity for optical interferometry measurement. Furthermore, Ag is a face-centered cubic crystal structure and Cr is a body-centered cubic crystal structure. The interface composed of the two different crystal structures has a strong ability to hinder dislocation motion [48].

Moreover, to improve the low-frequency response of the FP acoustic sensor, the electrical-mechanical-acoustic equivalent model was applied to the sensor design, as shown in Fig. 1(b). In the studied acoustic system, the size of each element is much smaller than the wavelength of the infrasound wave, which can be analyzed as a lumped system [49]. For a diaphragm-based

acoustic sensor, the diaphragm's performance can be easily affected by external environments such as temperature if the sensor cavity is closed, so an open cavity structure can eliminate the influence of external factors by making a connecting hole in the sensor cavity. However, the low-frequency acoustic pressure response of the sensor will be reduced due to the existence of the connecting hole. In the equivalent circuit model, the actual response of the acoustic sensor is determined by the sensitivity S_d of the diaphragm and the transfer function H. When the sensor is placed in an acoustic field with an acoustic pressure of p_{in}, only the acoustic pressure acting on the diaphragm can cause the deformation of the diaphragm, which is the effective acoustic pressure p_{out}. The ratio of p_{out} to p_{in} is defined as the transfer function H. The elements in Fig. 1(b) are the acoustic mass M_d of the diaphragm, the acoustic compliance C_d of the diaphragm, the radiation acoustic mass M_{rad} of the diaphragm, the radiation acoustic impedance R_{rad} of the diaphragm, the acoustic impedance R_{hole} of the connected hole, the acoustic mass M_{hole} of the balanced hole, and the acoustic compliance C_{cav} of the cavity. The complete electrical-mechanical-acoustic equivalent model is depicted in Appendix B. It can be seen from the transfer function expression that the low cut-off frequency f of the sensor can be expressed as follows:

$$f = \frac{1}{2\pi} \frac{C_{cav} + C_d}{C_d R_{hole}(1 + C_{cav}/C_d)}. \tag{2}$$

Figures 2(a) and 2(b) show the simulation results for the effect of connecting holes size on the transfer function. The presence of the connecting hole does not affect the sensor response in the flat area. However, in the low-frequency range, both the length and radius of the connecting hole greatly in-
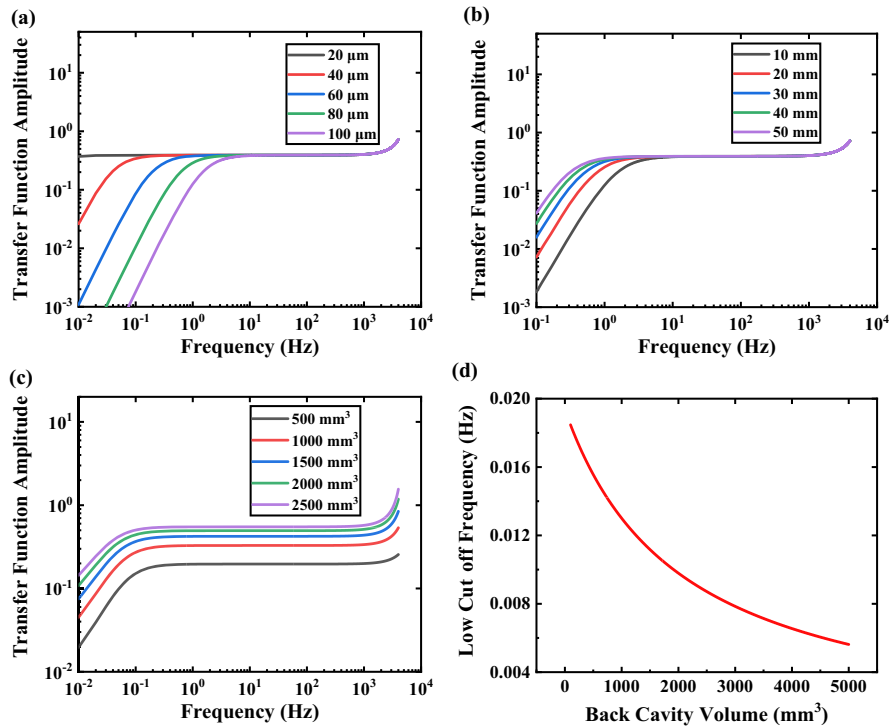

Fig. 2. (a) Effects of connecting hole radius on transfer function when connecting hole length is fixed. (b) Effects of connecting hole length on transfer function when connecting hole radius is fixed. (c) Effects of back cavity volume on transfer function. (d) Effects of back cavity volume on low cut-off frequency.

fluence the frequency response of the sensor. Specifically, shorter connecting hole length and larger connecting hole radius can result in more severe low-frequency attenuation. In addition, the effects of back cavity volume on the transfer function and low cut-off frequency are shown in Figs. 2(c) and 2(d), respectively. It can be seen that a large back cavity volume can lower the cut-off frequency, but a large back cavity volume means a large sensor size. Hence, to enhance the sensor's response sensitivity in the low-frequency band and minimize attenuation, it is recommended to increase the length of the connecting hole and decrease its radius as much as possible within the constraints of the structure and process, while ensuring that the sensor size does not increase.

3. EXPERIMENTAL SETUP AND RESULTS

A. Device Design

The MEMS technique was applied to the processing of the precision structures of the composite diaphragm. As shown in Fig. 3(a), the photoresist was used as the sacrificial layer in a silicon wafer and the electron beam evaporation process was adopted to complete the preparation of the high-performance composite metal diaphragms. The thickness was regulated to

20 nm, 500 nm, and 30 nm of Cr, Ag, and Au layers, respectively, by controlling the process parameters, and the density of the composite diaphragm was $10.856 \, \text{g/cm}^3$. A custom metal encapsulation was bonded to the composite diaphragm by epoxy glue and placed on a heating table for heating the epoxy glue to cure. The curing temperature was 80°C and the curing time was 60 min; then the diaphragm was transferred to the metal part by soaking in acetone. The effective sensing radius of the diaphragm was 4 mm.

To decrease the low cut-off frequency of the FP infrasound sensor, a design of a spiral micro-flow hole was proposed based on the MEMS technique, which can effectively increase the connecting hole length and reduce the sensor size, as shown in Figs. 3(b) and 3(c). First, the photoresist as a mask was coated on two silicon wafers. Second, the designed patterns of two mirror-symmetrical miniature grooves with a same diameter of about 48 µm were transferred to the photoresist in the two silicon wafers by photoetching, respectively. Third, the two grooves were etched on the two silicon wafers, respectively. The spiral shape extended the total length of each groove to 96.6 mm. Then the photoresist was cleaned off. Fourth, the starting point of one spiral groove and the end point of another spiral groove were etched into two through-holes by using the
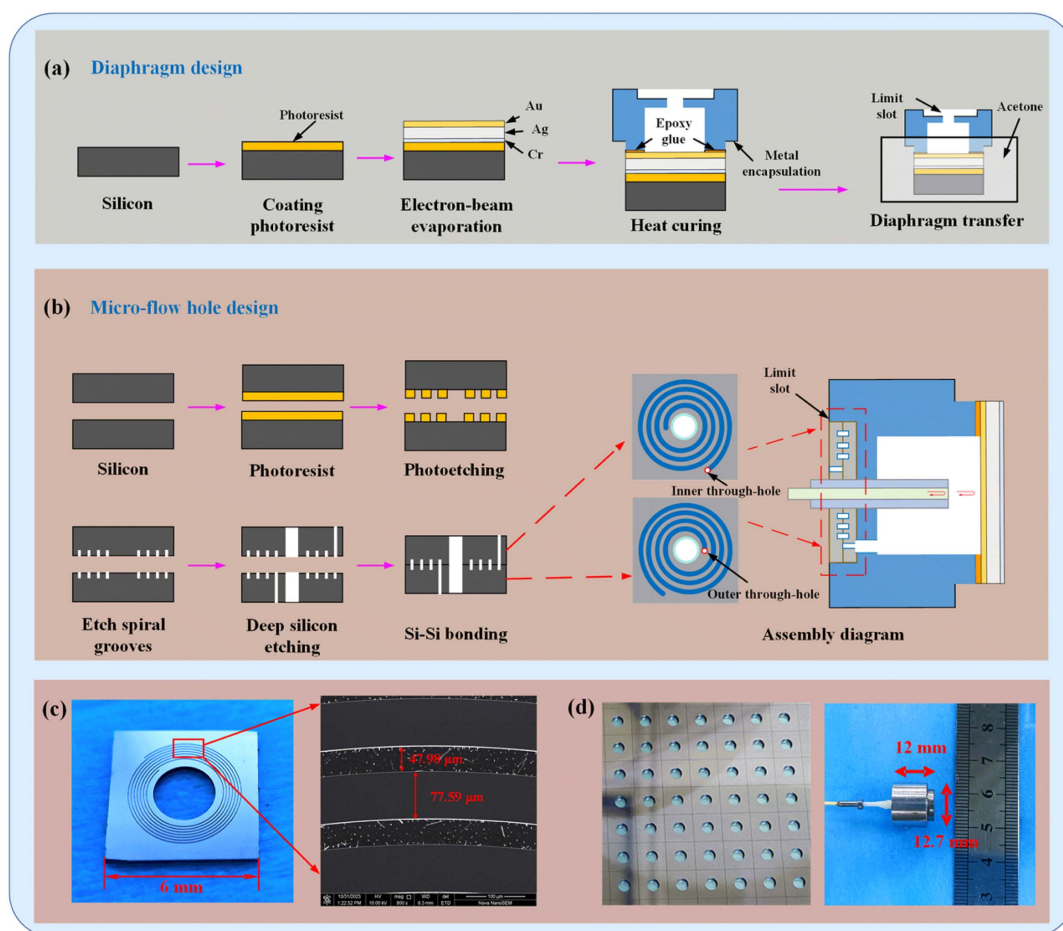

Fig. 3. (a) Fabrication process of the diaphragm. (b) Fabrication process of the spiral micro-flow hole and assembly of the sensor. (c) Left: picture of the single layer of silicon chip before bonding. Right: scanning electron microscope (SEM) image of the spiral groove structure. (d) Left: picture of the dual layers of large-area silicon wafers after bonding. Right: picture of the fiber-optic FP sensor.

deep silicon etching method, respectively. The through-holes for optical fiber penetration were simultaneously etched out. Finally, through the silicon–silicon bonding process for the two silicon wafers, the spiral micro-flow holes were formed by the mirror-symmetrical surface-etched spiral grooves inside two layers of silicon wafers. Due to the limitation of the silicon–silicon bonding process, two large-area silicon wafers were used in the above steps. Each small silicon chip with a size of 6 mm × 6 mm containing a spiral micro-flow hole was separated from the large-area silicon wafer by the slicing method after bonding. Figure 3(c) shows the picture of the single layer of silicon chip before bonding and the scanning electron microscope (SEM) image of the spiral groove structure. Figure 3(d) left shows the picture of the dual layers of large-area silicon wafers after bonding. A limit slot was designed on the metal encapsulation to fix the chip, as shown in Figs. 3(a) and 3(b). The physical picture of the completed fiber-optic FP sensor is displayed in Fig. 3(d) right. The volume of the packaged sensor back cavity is 417 mm^3.

B. Experimental Testing

According to the principle of acoustic metrology, we constructed an aeroacoustic testing system and conducted a performance test on the fiber-optic FP sensor, as shown in Fig. 4. Since the coupling cavity can suppress the low-frequency noise in the environment, we utilized the coupling cavity comparison method to measure the sensor response in the low-frequency band (0.01–100 Hz). Moreover, the free-field comparison method was employed to measure the sensor response in the high-frequency band (100 Hz to 5 kHz) due to the uneven distribution of acoustic field in the coupling cavity.

A C-band amplified spontaneous emission (ASE) light source module was implemented as the probe light source, with a wavelength range of 1526–1563 nm. Moreover, the WLI Fourier phase demodulation method was employed for acoustic signal extraction [50,51]. The ASE light was coupled into the fiber-optic FP sensor through a variable optical attenuator (VOA) and a fiber-optic circulator, and the reflected light signals were imported to a fiber Bragg grating analyzer (FBGA). The spectral signal was collected in real-time and input into the computer via the FBGA, which has a high sampling rate of 20 kHz to detect acoustic signals in a wider frequency range.

The spectral signals were then processed by a LabVIEW program that integrated a WLI demodulation algorithm to obtain the phase change information.

A low-frequency coupling cavity was used as an acoustic source for the sensor's low-frequency response measurement from 0.01 to 100 Hz. A commercial B&K 4193-L-004 microphone was exploited as the reference. Both the FP infrasound sensor and the reference microphone were simultaneously positioned at the two input ports of the low-frequency coupling cavity. To measure the high-frequency response from 100 Hz to 5 kHz, a commercial B&K 4190-L-001 microphone and a commercial speaker were used as the reference and the acoustic source, respectively. The FP infrasound sensor and the reference microphone were symmetrically placed on either side of the acoustic source axis at the free field with a distance of approximately 2.0 m from the test acoustic source. To reduce the influence of the environment, all experimental devices were placed in a fully anechoic chamber. When testing at both high frequency and low frequency, the signal generator of a B&K 3160-A-042 acoustic analyzer produced a sinusoidal signal and drove the test sound source to generate acoustic waves through a power amplifier with a gain of 18 dB. The output electrical signal of the reference microphone was collected and analyzed by the acoustic analyzer to obtain the value of test acoustic pressure. Furthermore, the detection sensitivity of the FP infrasound sensor can be obtained by the WLI Fourier phase demodulation algorithm. The photos of the sensor calibration system are shown in Appendix C.

C. Experimental Result

Figures 5(a)–5(c) show the measured frequency spectra of the sensor output signals by the WLI Fourier phase demodulation algorithm under the acoustic waves at 0.01 Hz, 0.05 Hz, and 0.1 Hz, respectively, which demonstrate the superior frequency resolution of the sensor. The demodulated 0.1 Hz acoustic signal with an excellent sine fitting, as shown in Fig. 5(d), means that the acoustic signal was accurately restored. In addition, the linear response of the sensor was also measured, as shown in Fig. 5(e). The linearity of the sensor reached 0.9999 at 5 Hz acoustic wave.

The measured acoustic pressure sensitivity of the sensor from 0.01 Hz to 5 kHz is shown in Fig. 6. The results indicate that
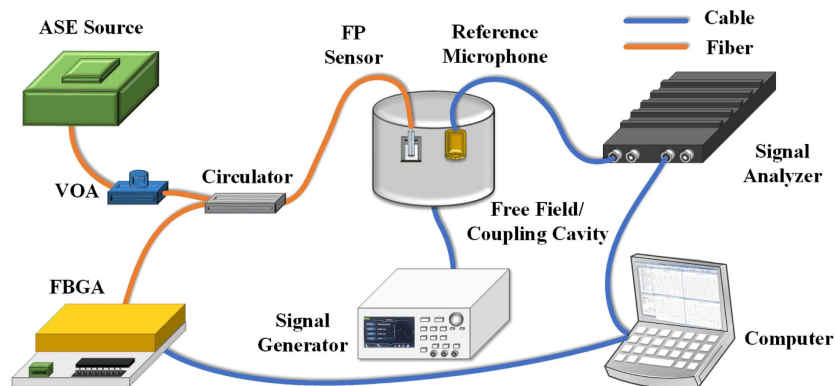

Fig. 4. Infrasound sensor calibration experimental system.
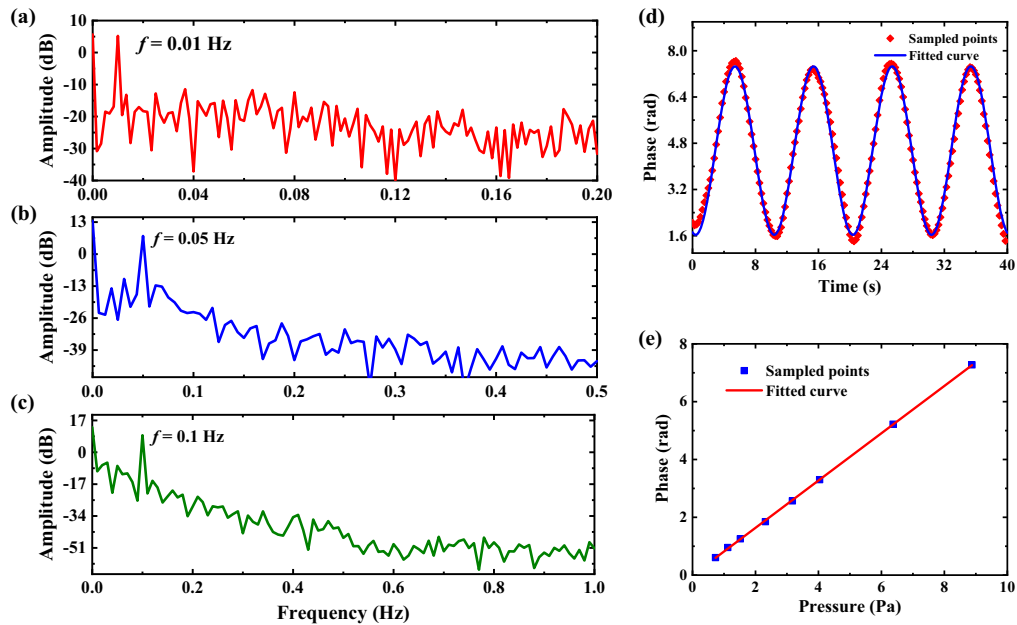
Fig. 5. Frequency spectra of the sensor output signals under the acoustic waves with different frequencies: (a) 0.01 Hz, (b) 0.05 Hz, (c) 0.1 Hz. (d) Sinusoidal fitting of time domain signal of 0.1 Hz. (e) Linearity of the sensor at 5 Hz acoustic wave.

the designed fiber-optic FP acoustic sensor can achieve 0.01 Hz acoustic detection and has a flat response from 0.01 to 2500 Hz with a sensitivity fluctuation of ±1.5 dB, while the average acoustic pressure sensitivity reached −123.19 dB re 1 rad/μPa at 5 Hz.
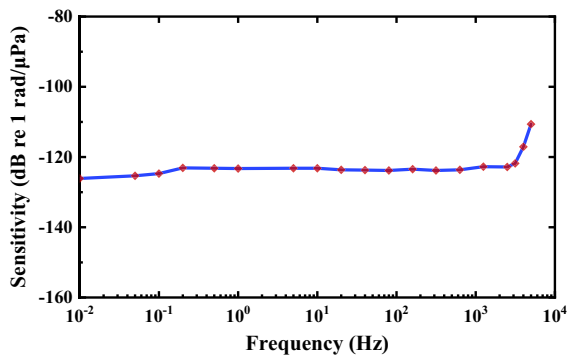

Fig. 6. Acoustic pressure sensitivity of the fiber-optic FP acoustic sensor from 0.01 Hz to 5 kHz.

The MDP is another critical index for an acoustic sensor, which is determined by both sensitivity and noise. To accurately assess the sensor noise characteristic, the sensor was placed in a fully anechoic chamber to effectively suppress the potential influence of environmental noise. The noise output signal, denoted as $n(t)$, was collected over a specific period. Subsequently, a frequency domain analysis of $n(t)$ was conducted, and the noise spectrum $N(f)$ was derived through Fourier transformation, as depicted in Fig. 7(a). Given that the total noise sampling time is T_s, the frequency spectrum abscissa point interval (or frequency resolution) $\Delta f = 1/T_s$ post-Fourier transformation. The MDP of the acoustic sensor with phase demodulation at each frequency can be calculated using Eq. (3). For instance, the MDPs were 1.2 mPa/Hz$^{1/2}$ at 5 Hz and 29.7 μPa/Hz$^{1/2}$ at 250 Hz. The MDPs under different frequencies are shown in Fig. 7(b):

$$\mathrm{MDP} = \frac{N(f)}{S(f)\sqrt{\Delta f}}\left[\frac{\mathrm{Pa}}{\mathrm{Hz}^{\frac{1}{2}}}\right]. \tag{3}$$
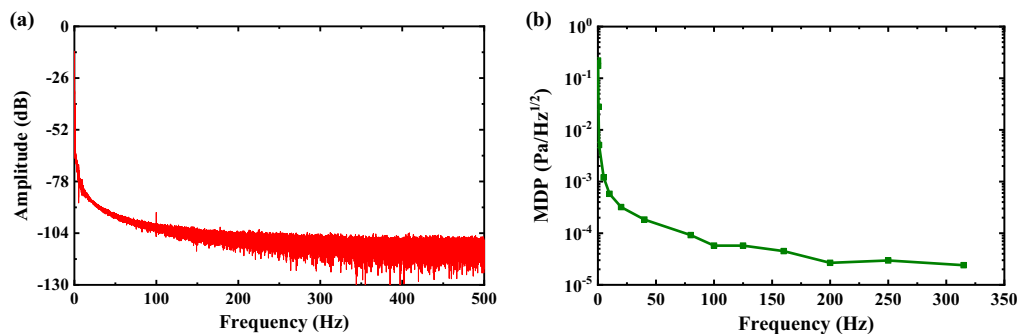

Fig. 7. Noise test results. (a) Noise spectrum, (b) minimum detectable pressure (MDP) under different frequencies.

Table 1.   Comparison between Different Fiber-Optic Infrasound Sensors

Diaphragm	Sensitivity	MDP	Frequency (Hz)	Reference
Silicon nitride	−152 dB re 1 rad/μPa at 100 Hz	/	0.1–250	[1]
Gold	−130.6 dB re 1 rad/μPa at 100 Hz	10.2 mPa/Hz$^{1/2}$ at 5 Hz	0.8–250	[28]
Silicon	−154.6 dB re 1 rad/μPa	/	10–2000	[44]
PPS (polyphenylene sulfide)	/	88.9 mPa/Hz$^{1/2}$	0.01–1	[46]
Cr-Ag-Au	**−123.19 dB re 1 rad/μPa at 5 Hz**	**1.2 mPa/Hz$^{1/2}$ at 5 Hz**	**0.01–2500**	**This work**

Compared with the currently reported fiber-optic infrasound sensor, the developed sensor in this work has a higher acoustic pressure sensitivity, a better MDP, and a lower detectable frequency. The comparison between different fiber-optic infrasound sensors is listed in Table 1.

4. CONCLUSION AND DISCUSSION

In conclusion, a fiber-optic FP infrasound sensor was designed and fabricated from principle to verification, which used a highly sensitive Cr-Ag-Au composite diaphragm as the acoustic-optic transducer diaphragm and a miniaturized MEMS spiral microflow hole with a total length of 96.6 mm as a connecting hole. The infrasound sensor achieved 0.01 Hz infrasound detection and a flat response from 0.01 to 2500 Hz with a sensitivity fluctuation of ±1.5 dB. The MDP reached 1.2 mPa/Hz$^{1/2}$ at 5 Hz and 29.7 μPa/Hz$^{1/2}$ at 250 Hz. Most importantly, the size of the developed infrasound sensor was only 12 mm × Φ12.7 mm. Hence, the sensor simultaneously achieved miniaturization, high sensitivity, mHz detectable frequency, and wide frequency response range. Due to the frequency limitation of the reference microphone, the frequency signal below 0.01 Hz was not detected, but it can also be responded in theory. Moreover, the all-fiber detection approach makes the sensor possess the advantages of all-optical passivity, intrinsic safety, immunity to electromagnetic interference, resistance to harsh environments, long-distance detection ability, and multiplexing ability. In practical applications, it is necessary to further optimize the strength of the diaphragm, and in the future, materials with high mechanical strength can be found as transducer diaphragms while ensuring a high sensitivity. Furthermore, the developed small-sized sensor is very convenient to integrate with other sensor devices to compose a multifunctional intelligent detection system. In addition, a sensor array can be formed due to the excellent consistency of the proposed MEMS-based fiber-optic infrasound sensor, and some corresponding algorithms can be combined to achieve the localization or orientation for the sound sources. This work provides a new idea and scheme for the military, disaster warning, pipeline leakage monitoring, and other fields.

APPENDIX A: PRINCIPLES OF THE DIAPHRAGM VIBRATION

Theoretical analysis of the forced vibration of the diaphragm is needed to select the appropriate material for the energy conversion diaphragm. According to the characteristics of the forced vibration of the diaphragm, the vibration equation can be obtained:

$$\nabla_r^2 \xi - \frac{1}{c^2} \cdot \frac{\partial^2 \eta}{\partial t^2} = -\frac{p}{c^2 \sigma}, \qquad \text{(A1)}$$

where η is the amount of displacement of the diaphragm, $c = \sqrt{T/\sigma}$, σ represents the areal density of the diaphragm, and T represents the tension of the diaphragm. When the diaphragm vibrates, the surrounding of the diaphragm is clamped, and the boundary condition of its vibration is $\xi_{(r=a)} = 0$, where r is the distance from the center of the circle and a is the radius of the diaphragm. The amount of displacement of the diaphragm can be obtained by solving the above equation, and the formula is expressed as follows:

$$\xi(t, r) = \frac{p_a}{k^2 T} \left[\frac{J_0(kr)}{J_0(ka)} - 1 \right] \cdot e^{j\omega t}. \qquad \text{(A2)}$$

In the formula, $k = \omega/c$, $J_0(kr)$ is the zeroth-order Bezier function. The maximum value of ξ can be obtained when $J_0(ka) = 0$. The resonant frequency equation for the forced vibration of the diaphragm and the first-order resonance frequency equation when the first-order root $\delta_1 = 2.405$ can be denoted as

$$f_n = \frac{\delta_n}{2\pi a} \sqrt{\frac{T}{\sigma}}, \qquad \text{(A3)}$$

$$f_1 = \frac{2.405}{2\pi a} \sqrt{\frac{T}{\sigma}}. \qquad \text{(A4)}$$

The formula above explains that the amount of displacement on a diaphragm when acoustic pressure is applied depends on its distance from the center. The edge experiences minimal displacement while the center experiences maximum. For FP sensors, the fiber end face must align with the center to determine the displacement sensitivity of the diaphragm by calculating the ratio of the shape variable at the midpoint to the acoustic pressure applied. The diaphragm's tension is $T = Ph$, where P represents the tensile stress and h represents the thickness, and the sensitivity can be expressed as Eq. (1) in the main text.

The simulation of the influence of various parameters on the diaphragm sensitivity is shown in Fig. 8. It can be seen that in order to improve the sensitivity of the diaphragm, it is necessary to reduce the tensile stress, increase the diameter, and reduce the thickness of the diaphragm. Considering that a diaphragm with a too large or too thin size is more fragile and prone to damage during practical use, a Cr-Ag-Au composite diaphragm with a radius of 4 mm and a total thickness of 550 nm was selected.

APPENDIX B: PRINCIPLES OF THE ELECTRICAL-MECHANICAL-ACOUSTIC EQUIVALENT MODEL

When studying acoustic sensors, the parameters in acoustics can be equivalent to those in circuits, and it is possible to
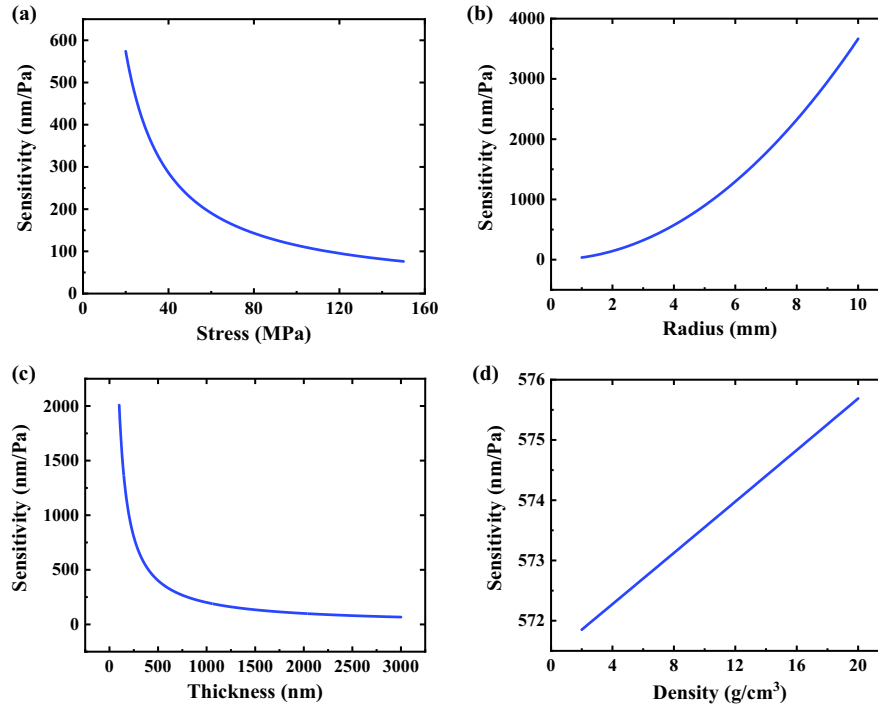
Fig. 8. Relationship between diaphragm sensitivity and various parameters. (a) Stress, (b) radius, (c) thickness, (d) density.

analyze the acoustic phenomenon by solving the equivalent circuit equation. But it should be noted that the electric acoustic equivalence model is mainly applicable to lumped systems, that is, the sizes of the acoustic objects (cavities, stubs, small holes, etc.) are much smaller than the wavelength of the acoustic wave. In the studied acoustic system, the size of each element is much smaller than the wavelength of the acoustic wave, which can be analyzed as a lumped system. For a diaphragm acoustic sensor, an open cavity structure with connecting holes can be used to eliminate sensor performance changes caused by external environments. However, the low-frequency response of the sensor will be reduced due to the connecting hole. In the equivalent circuit model, the actual response of the acoustic sensor is determined by the sensitivity S_d of the diaphragm and the transfer function H:

$$S_{fact} = H \cdot S_d. \tag{B1}$$

The internal structure and the equivalent circuit system of the proposed FP acoustic sensor are shown in Figs. 1(a) and 1(b), respectively, among them $Z_1 = R_{rad} + j\omega(M_d + M_{rad})$, $Z_2 = 1/j\omega C_d$, $Z_3 = 1/j\omega C_{cav}$, $Z_4 = R_{hole} + j\omega M_{hole}$. Therefore, the transfer function H can be expressed as

$$H = \frac{p_{out}}{p_{in}} = \frac{Z_2 Z_4}{Z_3 Z_4 + (Z_1 + Z_3)(Z_3 + Z_4)}. \tag{B2}$$

The lumped element definitions are shown in Table 2.

It can be seen from the transfer function expression that the sensing system has two resonance frequencies:

$$f_{high} = \frac{1}{2\pi}\sqrt{\frac{C_{cav} + C_d}{C_{cav} C_d (M_{rad} + M_d)}}, \tag{B3}$$

$$f_{low} = \frac{1}{2\pi}\frac{C_{cav} + C_d}{C_d R_{hole}(1 + C_{cav}/C_d)}. \tag{B4}$$

f_{high} is the resonant frequency, and f_{low} is the cut-off frequency of low frequency.

Table 2. Lumped Element Definitions

Model Parameter	Symbol	Definition[a]
Diaphragm acoustic mass	M_d	$\dfrac{4h\rho_f}{3\pi a^2}$
Diaphragm acoustic compliance	C_d	$\dfrac{\pi a^4}{8hP}$
Diaphragm radiation mass	M_{rad}	$\dfrac{8\rho_{air}}{3\pi^2 a}$
Diaphragm radiation resistance	R_{rad}	$\dfrac{\pi\rho_{air}c_{air}}{\lambda^2}$
Hole acoustic mass	R_{hole}	$\dfrac{8\varepsilon_{air}l_{hole}}{\pi a_{hole}^4}$
Hole radiation resistance	M_{hole}	$\dfrac{4\rho_{air}l_{hole}}{3\pi a_{hole}^2}$
Cavity acoustic capacity	C_{cav}	$\dfrac{V}{\rho_{air}c_{air}^2}$

[a] ρ_f is the density of the diaphragm, ρ_{air} is the density of air, c_{air} is the acoustic velocity of air, V is the volume of the back cavity, ε_{air} is the viscosity coefficient of air, a_{hole} is the radius of the connecting hole, l_{hole} is the length of the connecting hole, and λ is the wavelength of the acoustic wave.

APPENDIX C: ACOUSTIC TEST PHOTOS OF THE FIBER-OPTIC FP SENSOR

The photos of the sensor calibration system are shown in Fig. 9, including high-frequency testing and low-frequency testing, respectively.
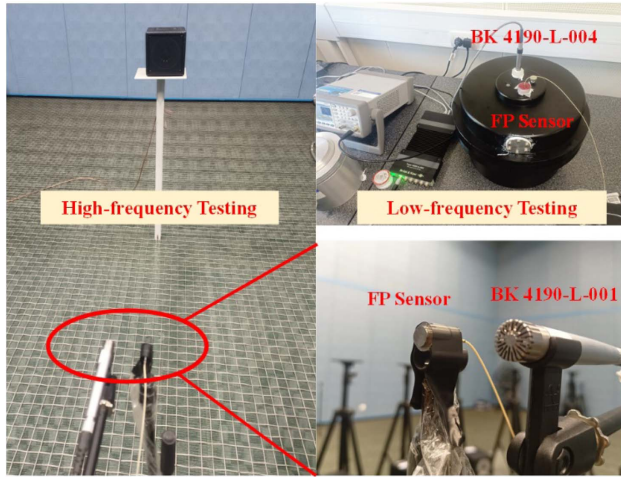

Fig. 9. Acoustic test photos of the fiber-optic FP sensor.

Disclosures. The authors declare no competing interests.

Data Availability. The data that support the findings of this study are available from the corresponding author upon reasonable request.

REFERENCES

1. Z. Qu, P. Lu, Y. Li, *et al.*, "Low-frequency acoustic Fabry–Pérot fiber sensor based on a micromachined silicon nitride membrane," Chin. Opt. Lett. **18**, 101201 (2020).
2. Y. Xia, J. T. Liu, X. Cui, *et al.*, "Abnormal infrasound signals before 92$M \geq 7.0$ worldwide earthquakes during 2002–2008," J. Asian Earth Sci. **41**, 434–441 (2011).
3. B. G. Gorshkov, A. E. Alekseev, M. A. Taranov, *et al.*, "Low noise distributed acoustic sensor for seismology applications," Appl. Opt. **61**, 8308–8316 (2022).
4. E. F. Williams, M. R. Fernández-Ruiz, R. Magalhaes, *et al.*, "Distributed sensing of microseisms and teleseisms with submarine dark fibers," Nat. Commun. **10**, 5778 (2019).
5. N. J. Lindsey, E. R. Martin, D. S. Dreger, *et al.*, "Fiber-optic network observations of earthquake wavefields," Geophys. Res. Lett. **44**, 11792–11799 (2017).
6. M. A. Garces, "Infrasonic signals generated by volcanic eruptions," in *IEEE International Symposium on Geoscience and Remote Sensing* (2000), pp. 1189–1191.
7. X. Leng, D. Liu, F. Wei, *et al.*, "Debris flows monitoring and localization using infrasonic signals," J. Mt. Sci. **14**, 1279–1291 (2017).
8. A. Schimmel and J. Hübl, "Automatic detection of debris flows and debris floods based on a combination of infrasound and seismic signals," Landslides **13**, 1181–1196 (2016).
9. J. B. Johnson, J. F. Anderson, H. P. Marshall, *et al.*, "Snow avalanche detection and source constraints made using a networked array of infrasound sensors," J. Geophys. Res. Earth Surf. **126**, e2020JF005741 (2021).
10. T. Thüring, M. Schoch, A. van Herwijnen, *et al.*, "Robust snow avalanche detection using supervised machine learning with infrasonic sensor arrays," Cold Reg. Sci. Technol. **111**, 60–66 (2015).
11. X. Cui, Y. Yan, Y. Ma, *et al.*, "Localization of CO_2 leakage from transportation pipelines through low frequency acoustic emission detection," Sens. Actuators A Phys. **237**, 107–118 (2016).
12. F. Tanimola and D. Hill, "Distributed fibre optic sensors for pipeline protection," J. Nat. Gas Sci. Eng. **1**, 134–143 (2009).
13. X. Zhang, F. Zhang, S. Jiang, *et al.*, "Short cavity DFB fiber laser based vector hydrophone for low frequency signal detection," Photonic Sens. **7**, 325–328 (2017).
14. W. Lv, M. Pang, Q. Shi, *et al.*, "Study on a fiber optic gradient hydrophone based on interferometer," Proc. SPIE **7156**, 71561E (2008).
15. J. G. V. Teixeira, I. T. Leite, S. Silva, *et al.*, "Advanced fiber-optic acoustic sensors," Photonic Sens. **4**, 198–208 (2014).
16. E. A. Silber, D. C. Bowman, and M. R. Giannone, "Detection of the large surface explosion coupling experiment by a sparse network of balloon-borne infrasound sensors," Remote Sens. **15**, 542 (2023).
17. W. Jo, O. C. Akkaya, O. Solgaard, *et al.*, "Miniature fiber acoustic sensors using a photonic-crystal membrane," Opt. Fiber Technol. **19**, 785–792 (2013).
18. J. Grangeon and P. Lesage, "A robust, low-cost and well-calibrated infrasound sensor for volcano monitoring," J. Volcanol. Geoth. Res. **387**, 106668 (2019).
19. Y. Chen, H. Wan, Y. Lu, *et al.*, "An air-pressure and acoustic fiber sensor based on graphene-oxide Fabry-Perot interferometer," Opt. Fiber Technol. **68**, 102754 (2022).
20. Y. Pan, P. Lu, L. Cheng, *et al.*, "Miniaturized and highly-sensitive fiber-optic photoacoustic gas sensor based on an integrated tuning fork by mechanical processing with dual-prong differential measurement," Photoacoustics **34**, 100573 (2023).
21. H. Wei, Z. Wu, K. Sun, *et al.*, "Two-photon 3D printed spring-based Fabry–Pérot cavity resonator for acoustic wave detection and imaging," Photonics Res. **11**, 780–786 (2023).
22. S. E. Hayber, T. E. Tabaru, S. Keser, *et al.*, "A simple, high sensitive fiber optic microphone based on cellulose triacetate diaphragm," J. Lightwave Technol. **36**, 5650–5655 (2018).
23. J. Wang, F. Ai, Q. Sun, *et al.*, "Diaphragm-based optical fiber sensor array for multipoint acoustic detection," Opt. Express **26**, 25293–25304 (2018).
24. J. Ma, Y. He, X. Bai, *et al.*, "Flexible microbubble-based Fabry–Pérot cavity for sensitive ultrasound detection and wide-view photoacoustic imaging," Photonics Res. **8**, 1558–1565 (2020).
25. X. Qi, S. Wang, J. Jiang, *et al.*, "Study on the sensitization effect of flywheel-like diaphragm on fiber-optic Fabry-Perot acoustic sensor," IEEE Access **8**, 99286–99293 (2020).
26. Y. Pan, J. Zhao, P. Lu, *et al.*, "All-optical light-induced thermoacoustic spectroscopy for remote and non-contact gas sensing," Photoacoustics **27**, 100389 (2022).
27. C. Li, H. Qi, X. Han, *et al.*, "Ultrahigh-speed phase demodulation of a Fabry-Perot sensor based on fiber array parallel spectral detection," Opt. Lett. **49**, 714–717 (2024).
28. P. Fan, W. Yan, P. Lu, *et al.*, "High sensitivity fiber-optic Michelson interferometric low-frequency acoustic sensor based on a gold diaphragm," Opt. Express **28**, 25238–25249 (2020).
29. B. Liu, J. Lin, H. Liu, *et al.*, "Extrinsic Fabry-Perot fiber acoustic pressure sensor based on large-area silver diaphragm," Microelectron. Eng. **166**, 50–54 (2016).

30. F. Xu, J. Shi, K. Gong, *et al.*, "Fiber-optic acoustic pressure sensor based on large-area nanolayer silver diaphragm," Opt. Lett. **39**, 2838–2840 (2014).
31. F. Guo, T. Fink, M. Han, *et al.*, "High-sensitivity, high-frequency extrinsic Fabry-Perot interferometric fiber-tip sensor based on a thin silver diaphragm," Opt. Lett. **37**, 1505–1507 (2012).
32. H. Li, X. Wang, D. Li, *et al.*, "MEMS-on-fiber sensor combining silicon diaphragm and supporting beams for on-line partial discharges monitoring," Opt. Express **28**, 29368–29376 (2020).
33. W. Wang, N. Wu, Y. Tian, *et al.*, "Miniature all-silica optical fiber pressure sensor with an ultrathin uniform diaphragm," Opt. Express **18**, 9006–9014 (2010).
34. X. Fu, P. Lu, J. Zhang, *et al.*, "Micromachined extrinsic Fabry-Pérot cavity for low-frequency acoustic wave sensing," Opt. Express **27**, 24300–24310 (2019).
35. Z. Gong, K. Chen, X. Zhou, *et al.*, "High-sensitivity Fabry-Perot interferometric acoustic sensor for low-frequency acoustic pressure detections," J. Lightwave Technol. **35**, 5276–5279 (2017).
36. S. Wang, J. Zhang, H. Xu, *et al.*, "An infrasound sensor based on extrinsic fiber-optic Fabry–Perot interferometer structure," IEEE Photonics Technol. Lett. **28**, 1264–1267 (2016).
37. W. Ni, P. Lu, X. Fu, *et al.*, "Ultrathin graphene diaphragm-based extrinsic Fabry-Perot interferometer for ultra-wideband fiber optic acoustic sensing," Opt. Express **26**, 20758–20767 (2018).
38. J. Ma, H. Xuan, H. L. Ho, *et al.*, "Fiber-optic Fabry–Pérot acoustic sensor with multilayer graphene diaphragm," IEEE Photonics Technol. Lett. **25**, 932–935 (2013).
39. H. Moradi, P. Parvin, A. Ojaghloo, *et al.*, "Ultrasensitive fiber optic Fabry Pérot acoustic sensor using phase detection," Measurement **172**, 108953 (2021).
40. F. Yu, Q. Liu, X. Gan, *et al.*, "Ultrasensitive pressure detection of few-layer MoS₂," Adv. Mater. **29**, 1603266 (2017).
41. S. Li, Y. Zhang, C. Ma, *et al.*, "MEMS optical fiber F–P hydrophone based on corrugated PET diaphragm," IEEE Trans. Instrum. Meas. **72**, 7001710 (2023).
42. B. Liu, H. Zhou, L. Liu, *et al.*, "An optical fiber Fabry-Perot microphone based on corrugated silver diaphragm," IEEE Trans. Instrum. Meas. **67**, 1994–2000 (2018).
43. W. Yang, L. Jin, Y. Liang, *et al.*, "Corrugated-diaphragm based fiber laser hydrophone with sub-100 µPa/Hz^(1/2) resolution," Sensors-Basel **17**, 1219 (2017).
44. F. Wang, Z. Shao, J. Xie, *et al.*, "Extrinsic Fabry–Pérot underwater acoustic sensor based on micromachined center-embossed diaphragm," J. Lightwave Technol. **32**, 4628–4636 (2014).
45. O. Marcillo, J. B. Johnson, and D. Hart, "Implementation, characterization, and evaluation of an inexpensive low-power low-noise infrasound sensor based on a micromachined differential pressure transducer and a mechanical filter," J. Atmos. Ocean. Tech. **29**, 1275–1284 (2012).
46. P. Zhang, S. Wang, J. Jiang, *et al.*, "Mechanical filter-based differential pressure fiber-optic Fabry-Perot infrasound sensor," IEEE Photonics J. **13**, 6800110 (2021).
47. W. Zhang, P. Lu, Z. Qu, *et al.*, "High sensitivity and high stability dual Fabry-Perot interferometric fiber-optic acoustic sensor based on sandwich-structure composite diaphragm," IEEE Photonics J. **13**, 710113 (2021).
48. Y. P. Li, G. P. Zhang, W. Wang, *et al.*, "On interface strengthening ability in metallic multilayers," Scr. Mater. **57**, 117–120 (2007).
49. S. Lorenzo, Y. Wong, and O. Solgaard, "Optical fiber photonic crystal hydrophone for cellular acoustic sensing," IEEE Access **9**, 42305–42313 (2021).
50. X. Fu, P. Lu, W. Ni, *et al.*, "Phase demodulation of interferometric fiber sensor based on fast Fourier analysis," Opt. Express **25**, 21094–21106 (2017).
51. K. Chen, Z. Yu, Q. Yu, *et al.*, "Fast demodulated white-light interferometry-based fiber-optic Fabry-Perot cantilever microphone," Opt. Lett. **43**, 3417–3420 (2018).